Received: 3 January 2022 | Revised: 18 May 2022 | Accepted: 7 June 2022

DOI: 10.1002/qua.26964

RESEARCH ARTICLE

International Journal of Quantum Chemistry WILEY

Understanding proton transfer in non-aqueous biopolymers based on helical peptides: A quantum mechanical study

Jiang Bian[1,2] | Anthony Cruz[1,2] | Gabriel López-Morales[1,2] | Anton Kyrylenko[1] | Donna McGregor[1,2] | Gustavo E. López[1,2]

[1]Department of Chemistry, Lehman College of the City University of New York, Bronx, New York, USA

[2]Department of Chemistry, The Graduate Center of the City University of New York, New York, New York, USA

Correspondence
Gustavo E. López, Department of Chemistry, Lehman College of the City University of New York, Bronx, NY 10468, USA.
Email: gustavo.lopez1@lehman.cuny.edu

Funding information
NIH/SCORE, Grant/Award Number: 1SC3GM139673; NSF CREST Center for Interface Design and Engineered Assembly of Low Dimensional Materials (IDEALS), Grant/Award Number: HRD-1547830

Abstract

Histidine (an imidazole-based amino acid) is a promising building block for short aromatic peptides containing a proton donor/acceptor moiety. Previous studies have shown that polyalanine helical peptides substituted at regular intervals with histidine residues exhibit both structural stability as well as high proton affinity and high conductivity. Here, we present first-principle calculations of non-aqueous histidine-containing 3_{10}-, α-, and π-helices and show that they are able to form hydrogen-bonded networks mimicking proton wires that have the ability to shuttle protons via the Grotthuss shuttling mechanism. The formation of these wires enhances the stability of the helices, and our structural characterizations confirm that the secondary structures are conserved despite distortions of the backbones. In all cases, the helices exhibit high proton affinity and proton transfer barriers on the order of 1–4 kcal/mol. Zero-point energy calculations suggest that for these systems, ground state vibrational energy can provide enough energy to cross the proton transport energy barrier. Additionally, ab initio molecular dynamics results suggests that the protons are transported unidirectionally through the wire at a rate of ~2 Å every 20 fs. These results demonstrate that efficient deprotonation-controlled proton wires can be formed using non-aqueous histidine-containing helical peptides.

1 | INTRODUCTION

Over the past decade, proton transport has been extensively studied because of its many applications in the development of new technological devices. In particular, understanding proton transport permits the design of new materials that can be used for the construction of more effective proton exchange membranes (PEM) in fuel cells. Current PEM technology involves the use of expensive perfluorinated membranes. Two main limitations arise when using these membranes: (i) proton conductivity is heavily affected by the water content, which is in turn affected by the relatively high temperatures where fuel cells operate, and (ii) upon membrane degradation perfluorinated compounds, which are toxic and bioaccumulate, are released into the environment [1, 2]. The development of alternative and more environmentally friendly proton-conducting materials that can form proton wires and operate through a non-aqueous and non-solvent mediated mechanism are thus relevant. Conventional fuel cell designs show that, to be effective, proton conduction should happen quickly, selectively, and unidirectionally. The design of these new PEM materials then requires a fundamental understanding of how the protons might migrate through the structure in a non-solvent-mediated mechanism.

Amphiprotic molecules, which act as both proton donor and proton acceptor moieties (where protons can translocate from one part of the molecule to another), permit the transport of protons through a material independently of a solvent. The mechanism proposed for this proton translocation is called the Grotthuss shuttling mechanism (GSM) [3–5]. Here, protons typically translocate along a chain of hydrogen-bonds

(H-bonds) formed by the amphiprotic molecules, with the formation and cleavage of H-bonds occurring between neighboring molecules separated by distances of ~5–6 Å [6]. These structures can then effectively act as non-aqueous proton wires. The rate of proton migration depends on the details of the energetics defined by a translocation coordinate between the molecules donating and accepting the protons. Previous computational work by Viswanathan et al. has shown that non-aqueous tethered hydrogen-bonded chains formed of HX (X = imidazole, triazole, formic, sulfonic, or phosphonic acids) tend to be stabilized by strong H-bonds (up to 12 kcal/mol), with bond strength correlated to the proton affinity [6]. In addition, they predicted that interdigitated wires would produce faster conduction than linear wires for tethered imidazole- and triazole-based proton wires.

Recently, experimental studies have shown the development of non-aqueous materials by the addition of amphoteric species to well-known proton conducting membranes. Li et al. designed and synthesized a new polybenzimidazole (Tp-DADMB) anhydrous proton conducting material with a two-dimensional microporous structure [7]. This material was loaded with imidazole molecules in its nano-space and exhibited a proton conductivity of 2.4×10^{-3} S/cm at 130°C, making it suitable for use in the PEM. Sen et al. studied thermally stable Nafion-based proton-conducting anhydrous composite membranes under high temperatures composed of Nafion/1H-1,2,4-Triazole, Nafion/3-amino-1,2,4-triazole, and Nafion/5-amino-tetrazole [8]. They found that these systems have high proton conductivity (10^{-3} S/cm) at 180°C in the anhydrous state.

The amino acid histidine (His, an amphiprotic species) possesses proton donor/acceptor capabilities via the two nitrogen atoms (N) in the imidazole ring. Moreover, His-containing materials can be synthesized in helical secondary structures, which could favor the formation of proton wires. Additionally, the macroscopic electric dipole moment that helical peptides possess could facilitate the unidirectional proton translocation through the amphiprotic side chains of the peptides.

Although several molecular modeling studies have shed light on proton transport in bulk and confined water, very little is known about the fundamentals of proton conduction in non-aqueous systems [9]. We have previously reported [10] ab initio calculations on three 21-residue helical His-containing peptides forming 3_{10}-, α-, and π-helical secondary structures and found that all helices are stable and possess high proton affinities. Further, we concluded that the Grotthuss-shuttling proton transfer mechanism could occur with barriers ranging from 2 to 5 kcal/mol. The present study is a comprehensive extension of our previous work. In our prior study, we established that proton transfer was possible in a 21-residue His-containing peptide in 3_{10}-, α-, and π-helices but provided no structural, mechanistic, nor dynamical details. Here, we gain deeper insight into the fundamental requirements of proton transfer for His-containing peptides of varying lengths for the same 3_{10}-, α-, and π- secondary structures. While it is known that α-helices are the common helical secondary structure, it has been shown that certain amphiprotic moieties self-assemble into composites that resemble 3_{10}- and π-helices [11]. Hence, there is a need to consider these secondary structures (Figure S1). In this study, we are modeling the proton-conducting capabilities of non-aqueous proton wires built from various His-containing helical peptides with different characteristics, that is, size/length and secondary structure. We characterize in detail the translocation of a proton through His-based helical peptides and demonstrate that the proton translocation is fast and occurs potentially unidirectionally (a translocation of 2 Å approximately every 20 fs in the direction of the helical axis). Moreover, this work establishes the parameters required for the design of proton wires by better understanding what controls proton adsorption, diffusion, and desorption.

2 | COMPUTATIONAL METHODS

The proton-conducting capabilities of three major helical polypeptide chains formed from α-amino acids were investigated under non-aqueous conditions, with all calculations being done in the gas phase. Understanding proton transfer through a non-aqueous wire requires a fundamental understanding of (1) proton affinity, (2) deprotonation, and (3) diffusion through the wire, in each case with no implicit or explicit solvent. We focus on the making and breaking of H-bonds, which from a computational point of view are accurately described by ab initio calculations [11, 12]. We began by optimizing all structures and possible transition states studied in order to construct the potential energy landscapes for proton translocation. The relative stability of each structure is estimated by calculating the energy required to form the wire from the constituent starting components, and the difference in energy between the pure alanine (Ala) and the His containing peptides is then defined as the wire energy (WE). Finally, we look at the dynamics of proton transfer and the possibility of unidirectional proton translocation using ab initio molecular dynamics.

The helices were constructed by substituting His at regular intervals in three different poly-Ala helical peptide chains. Specifically, the following 18 helices were built: (i) 3_{10}-helices with sequence $Ala_3(His\text{-}Ala_2)_x$, ($x = 2$–7), (ii) α-helices with sequence $Ala_2(His\text{-}Ala_3)_yHisAla_2$, ($y = 1$–6), and (iii) π-helices with sequence $Ala_2(His\text{-}Ala_4)_zHisAla_3$, ($z = 1$–6). These sequences were chosen because of the well-known fact that helical poly-Ala are stable systems.

The 18 initial unprotonated helical structures were generated using BIOVIA Discovery Studio 3.5 [13]. The secondary structures of each helix were confirmed by computing the phi (φ) and psi (ψ) angles, that is, 3_{10}- with $\varphi = -74$ and $\psi = -4°$, α- with $\varphi = -57.8$ and $\psi = -47°$, and π-with $\varphi = -57.1$ and $\psi = -69.7°$. The N-terminus was capped with an acetyl group, and the C-terminus with an NH_2 group, thus rendering uncharged peptides. The structures are constructed so that the side chains of the rotamers are aligned to be parallel to one other, which is the least biased structure with respect to the formation of the wire. We called these systems the initial helical structures, and in Figure S1 an example of the three type of helixes containing seven His residues are shown.

All structures were computationally studied using the two-layer ONIOM formalism where a hybrid approach was implemented by combining density functional theory (DFT) and a semi-empirical molecular orbital method, that is, the His-side chains where proton transport occurs were treated using B3LYP with the 6-311G(d,p) basis set, and the rest of the system was modeled using the semi-empirical AM1 method. Within this hybrid B3LYP/AMI approach, the total energy of the system for each helical peptide was calculated by adding the energy of the different components of the layers:

$$E = E_{\text{low}}^{\text{full}} + E_{\text{high}}^{\text{subset}} - E_{\text{low}}^{\text{subset}} \tag{1}$$

in which low and high refers to AM1 and B3LYP/6-31G(d,p) methods, respectively, and full and subset refers to the partitioning of the system, that is, full is the entire peptide chain, and the subset is the His-side chains (β-carbon, hydrogens on the β-carbon, and the imidazole). For each unprotonated helix, the lowest energy structure was obtained by doing a full geometric optimization in the vapor phase. Specifically, the $3N - 6$ ($N =$ number of atoms) internal coordinates were optimized using the constructed initial helical structures.

A harmonic vibrational analysis was then performed on the optimized structures obtained to ensure that a minimum in the potential energy landscape (PEL) was identified. Additionally, the zero-point vibration energy (ZPE) was obtained from this harmonic vibrational analysis. All calculations were performed using Gaussian 09 [14].

To characterize the structure of the helices considered, various properties were calculated using the TRAJELIX module within the SIMULAID [15, 16]. Quantities computed include the length of the helices per residue (LEN), turn angle per residue (TPR), and root mean square (RMS) deviation with respect to the initial helical structure. The LEN of the helix was measured by considering the first amino acid residue from the N-terminus to the last residue without caps on the C-terminus. The calculation output from TRAJELIX was validated by comparing the RMS and TPR values of the initial helical structures with the reported values from Mezei et al. [15] In addition, we calculated the bend angle of each helix, and used the initial helical structure with zero degrees of bending as reference. The bend angle was computed in the following way. The helix was divided into two segments; the first half started from the N-terminus and was aligned with the initial helix. The number of residues forming this first half was determined by minimizing the root mean square deviation (RMSD) with respect to the initial helix. For example, when aligning the optimized unprotonated 3_{10}- helix with 7 His residues, $Ala_3(His\text{-}Ala_2)_7$, with its initial reference, we visually noticed using PyMOL [17] that helical bending occurred around the 16th amino acid residue. We selectively aligned segments composed of (i) residue 2–15, (ii) residue 2–16, and (iii) residue 2–17, with the corresponding segments of the reference, and obtained RMSD values of 2.1, 1.5, and 2.1, respectively. Hence, the first segment was defined from residues 2–16. The second segment was defined to be the remaining amino acids of the sequence (in the given example, it was residues 17–24). After defining the two segments of the peptide, the coordinates of the helical axis (S and E coordinates as calculated by TRAJELIX)) were obtained for the two segments. The bend angle of each individual helix was then defined as the angle between the two segments. This method was applied for all 18 helices and their protonated forms (for a total of 99 structures).

The stability [10] of each capped helix relative to its constituents was determined by computing the polymerization energy based on the reaction:

$$(M-N)\text{Ala} + N\text{His} + \text{Acetic Acid} + \text{Ammonia} \rightarrow \text{Acetyl} - (\text{Ala})_{M-N}(\text{His})_N\text{NH}_2 + (N+1)\,\text{Water} \tag{2}$$

For this reaction:

$$\Delta E = E_{\text{Peptide}} + (N+1)E_{\text{Water}} - E_{\text{Acetic Acid}} - E_{\text{Ammonia}} - (M-N)E_{\text{Ala}} - NE_{\text{His}} \tag{3}$$

where N is the number of His residues in the peptide and M is the total number of amino acids forming the helix. The ammonia and acetic acid are used for capping the terminals, and the water molecules in the product are released from the formation of the peptidic bonds. The value of each energy term was extracted from a single-point energy calculation at the B3LYP/6-311G(d,p) level using the ONIOM optimized structure. The polymerization energies were computed for all the unprotonated helices (ΔE_{His}) studied and pure poly-Ala (ΔE_{Ala}) helices with the same number of residues as the poly-His of interest. The poly-Ala provided information about the stability of each poly-His helix due to the formation of a proton wire. Because pure poly-Ala helixes do not form hydrogen bonds between the side-chains, the difference in energy between the pure Ala and the His containing peptides was defined as the wire energy (WE), which gives the stability of the system due to the wire formation.

Further energetics of the protonated systems were characterized by computing parameters such as proton affinity (PA) and deprotonation energy (DE) for each structure, defined as:

$$\text{PA} = E_{\text{optimized unprotonated structure}} - E_{\text{optimized protonated structure}} \tag{4}$$

$$\text{DE} = E_{\text{initial unoptimized protonated structure}} - E_{\text{final optimized protonated structure}} \tag{5}$$

PA > 0 and measures the tendency of a system to be protonated. Similarly, DE > 0, and is the energy required for the proton to be released from a particular helix site. PA and DE were computed by adding a proton to the N-terminus or extracting a proton from the C-terminus, respectively. Figure S2 shows a representation of how a proton is added to compute PA, and how it is removed to obtain DE.

To understand the PEL of proton transfer for each system, an excess proton was added to the first His encountered (labeled His_1) in the primary sequence starting from the N-terminus of the helical peptide chain. In order to simulate the Grotthuss shuttling mechanism, the proton was manually moved to His_2, His_3, His_4, and so on until the protonation reached the last His (closest to the C-terminus). Similar to the unprotonated species, a full geometry optimization was performed for each of these protonated systems, followed by the harmonic vibrational analysis. Additionally, transition states (TS) between two consecutive His residues were constructed by placing the excess proton between the delta-nitrogen (δN) of one His and the epsilon-nitrogen (εN) of the adjacent His. In this case, the transition state was found by using the Berny algorithm [18] as implemented in Gaussian 09. In the case of the transition state, one imaginary frequency in the vibrational analysis was used to confirm the nature of the minima. Based on these protonated structures, we defined the reaction coordinate along the axis where the proton is translocated, and hence energy vs. reaction coordinate curves (termed potential energy curves, PEC) were constructed to characterize the proton translocation processes. The methods employed here are similar to those employed to study proton translocation by other groups in similar systems [19–22].

To further understand the proton translocation mechanism in helical peptides from a dynamical point of view, ab initio molecular dynamics (AIMD) simulations were performed for the α-helix with four and seven His residues, that is, $Ala_2(His\text{-}Ala_3)_nHisAla_2$., $n = 3$ and $n = 6$. Specifically, AIMD were performed within the projector-augmented wave (PAW) methodology as implemented in VASP [23, 24]. The Brillouin zone was sampled using the Γ-point only, with a plane-wave cutoff of 400 eV for the construction of the basis set. To ensure electronic convergence, the electronic loops along the AIMD simulation were stopped when changes in energy were less than 10^{-6} eV. Exchange-correlation interactions were treated using the Perdue–Burke–Ernzerhof (PBE) functional [25] with Van der Waals (VdW) corrections introduced via the zero-damping scheme of Grimme DFT + D3 [26]. These VdW corrections are included to properly treat H-bonds within the protonated peptides. To protonate the peptide effectively, the overall electrostatic charge of the supercell was kept in a + 1 state during the simulation. The temperature was set to 300 K and kept constant during the simulation. A time step of 1 fs was used. The $Ala_2(His\text{-}Ala_3)_3HisAla_2$ was run for 1.0 ps, whereas $Ala_2(His\text{-}Ala_3)_6HisAla_2$ was run for 1.1 ps. Because of the computational demands of these simulations, longer runs were not possible with the available computer resources.

The proton translocation was quantified by computing a proton sharing coordinate defined by $\delta_{x-y} = d_1 - d_2$ where d_1 is the distance between the δN of His_y and the H on the adjacent His_x (initially forming a H-bond) and d_2 is the distance between the εN in His_x and its (initially) covalently bound H. At $t = 0$ fs, $\delta_{x-y} > 0$, in the transition state $\delta_{x-y} = 0$, and upon proton translocation $\delta_{x-y} < 0$. During the MD simulation δ_{x-y} was monitored as a function of time. Figure S3 shows a representation of two adjacent Hises residue and how the proton sharing coordinate is computed.

3 | RESULTS AND DISCUSSION

Our results are organized as follows. In Section 3.1, the structural properties of the helices are discussed. In Section 3.2, the energetics and stability of the systems are discussed. In Section 3.3, the PEC for the proton translocation are presented along with AIMD results for two of the α-helices.

3.1 | Structural properties

The unprotonated optimized lowest energy structures for the 3_{10}-, α-, and π-helices for the systems containing seven His residues are shown in Figure 1A–C, respectively. The helices containing seven His-residues (Figure 1A–C, top panel) are chosen as an example of the optimized structures, but similar geometries are obtained for the same type of helices 2, 3, 4, 5, and 6 His (see Figure S4). The secondary structure panels (Figure 1A–C bottom left) show that each of the systems studied conserved the helical secondary arrangement. The helical wheel representations for each optimized structure are shown in the bottom right of Figure 1A–C with the wheel representations for the initial structures above the helical wheels for the optimized structures. Figures S5 and S6 show the helical wheels for all the omptimes helices studied. The optimized structures show wheels with the His residues located on one side of the cylinder and a distortion in the cylindrical axis. Specifically, in the case of the α- and π-helices, the His residues that were distributed on the entire external surface moved to align on a single side. In the case of the initial 3_{10}-helix, the His residues were already on one side of the helical cylinder, hence the movement of the His residues was less pronounced. This alignment of the His residues is responsible for the formation of a wire-like structure that is linked by a H-bonded network formed between the protonated-deltaN (p-δN) of one His and the unprotonated-epsilonN (u-εN) of the adjacent His.

Various structural properties for the optimized structures and the initially constructed 3_{10}-, α-, and π-helices are shown in Table 1. The data for all helices studies are shown in Table S1. Because our results show that the properties are-independent of the number of His contained in the peptide, average values for TPR, the angle between adjacent His, θ, and the LEN over all unprotonated and protonated states (which have minimal variations in the structures) are reported for each type of helices. Values for individual helices are shown in Supporting Information. For the p-δN

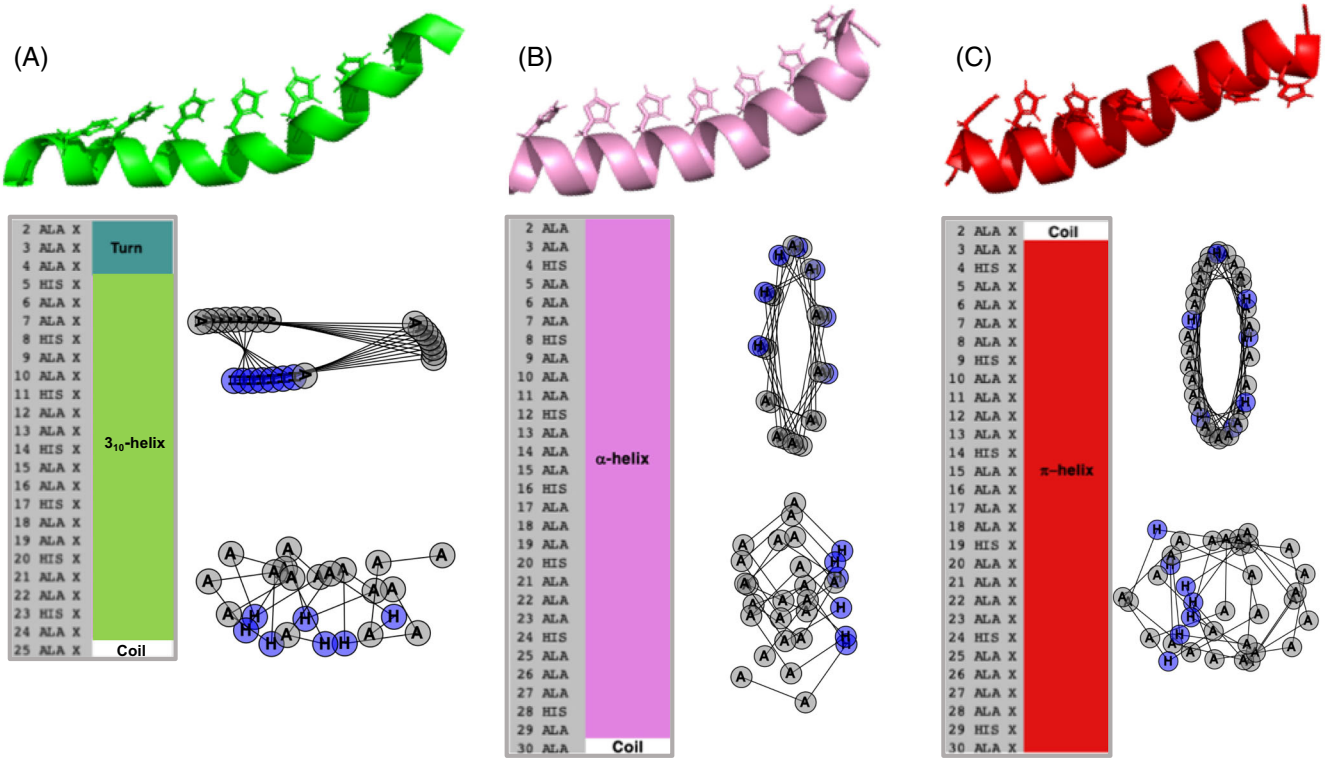

FIGURE 1 Representations of the fully optimized unprotonated (A) 3_{10}- (green), (B) α- (pink), and (C) π-helices (red) with seven His. Panels on the bottom left in each case show the corresponding secondary structure with the wheel diagrams on the bottom right showing the specific alignment of the His residues (shown in blue). The helical wheels for the initial helices are included above those for the optimized structures.

TABLE 1 Summary of the average distance between the H in the p-δN and the u-εN of adjacent His residues (*B*), the angle between adjacent His (θ) the LEN and the turns per residues (TPR) for the 3_{10}-, α-, and π-helices

Helix	System	TPR (degrees)	*B* (Å)	θ (degrees)	LEN (Å)
3_{10}	Initial	118	5.95	4	2.1
	Optimized	112	2.02 (2)	32 (7)	1.6 (1)
α	Initial	98	5.76	20	1.7
	Optimized	89	2.02 (7)	31 (13)	1.3 (1)
π	Initial	83	6.18	38	1.2
	Optimized	77	2.11 (4)	26 (3)	1.1 (1)

Note: TPR, θ, and the LEN for the optimized systems were calculated by averaging over all protonated and unprotonated structures of all sizes. For the p-δN and the u-δN bond distances only the unprotonated systems were considered. The number in parenthesis is the uncertainties in the last decimal place of the computed averages.

and the u-εN bond distances only the optimized unprotonated structures were averaged because upon protonation the His residue that is protonated exhibits a p-δN and u-εN bond distance on the order of 1.6–1.7 Å. This occurs in all systems studied.

The third column in Table 1 shows the average turn per residue (TPR) for each system. When comparing these with the initial helices, we see only small changes in the TPR (<10%), which supports the conservation of the secondary helical structures after optimization. The fourth column shows the average distance between the H in the p-δN and the u-εN of adjacent His residues. In the initial structures, this distance is about 6 Å in length, but in the optimized structure this distance closes to 2.02 Å for the 3_{10}- and α- helices, and 2.11 Å for the π-helices. The closure of this distance to about 2 Å indicates the formation of a H-bond network upon optimization. We have characterized the alignment of the His residues by computing the angles between adjacent His, θ, that is, the angle between unitary vectors originating in the center of the imidazole rings in two adjacent His. The fifth column in Table 1 shows θ for both the initial and optimized helices, and it is observed that θ for all optimized helices is ~30°, with a large change (28^0) being observed for the 3_{10}-helix when compared with the initial structure. In the case of the α- and π-helices, θ increases by 11° and decreases by 12°, respectively, from the initial structure.

Table 1 also shows the length of the helix per residue (LEN, last column). When comparing these with the initial helices, the 3_{10}- and α-helices show a 27% decrease in LEN, whereas the π-helix is shortened by only 9%. These results support the previously observed distortion of the helix upon optimization.

Based on the p-δN and the u-εN bond distance and θ calculated for adjacent His residues, the three different types of helices are shown to be forming a network of hydrogen bonds that results in the formation of structurally similar proton wires. The formation of these wires suggests that a proton can be transported through the His residues following a Grotthuss shuttling mechanism [4]. Details about the proton translocation are discussed in Section 3.3.

In order to characterize the previously noted helical distortions, superimposed structures of the initial helices and the optimized unprotonated and protonated helices with seven His are shown in Figure 2. A similar figure for all other helices studied are shown in Figure S4. As previously stated, protonated equilibrium structures were obtained by sequentially adding the proton to each His. It can be observed from Figure 2 that there is a significant bending of the backbone of the optimized unprotonated and all protonated structures with respect to the initial helices. The degree of bending depends on the nature of the helix, and the bend angle does not significantly change upon protonation.

It should be noted that optimization of the initial structure obtained from the vapor calculations results in the aforementioned bending of the helix, but optimization of the initial structure with implicit water does not. If the vapor phase bent structure is solvated however, the bend in the helix is conserved upon optimization, indicating that this is a viable structure. Because we are interested in studying non-aqueous systems and there is experimental evidence to show that helical peptides can be bent in the solid state [27], we are choosing to explore the bent structure in this study.

Figure 3 shows the bending angle as a function of size for the three helix types in the vapor phase. In all cases, the bend angle increases as length increases, with the α- and π-helices behaving similarly; their bend angles are almost identical until the helix has six His. For the seven-His helices, 3_{10}- has a bend angle of 51°, α- 39°, and π- 29°. Despite these large bending angles, the secondary structures remain unchanged. It is important to note that helical bending similar to what we observe here has recently been observed for 18-residue peptides [27]. These peptides are similar to ours in that they exhibit a helical conformation and show bending angles that vary from 40.8° to 59.9°. This bending of the helix (observed both by us and in the literature) suggests that there might be multiple modes of peptide aggregation, and this could, in turn, result in nucleation and growth of potentially well-ordered structures that can be designed for specific applications.

3.2 | Stability and energetics

The stability of the helices was determined by calculating the polymerization energy using Equation (3). Table 2 shows the polymerization energy for all the helices studied as a function of size, with respect to the number of His residues. Included are the polymerization energies of the poly-Ala helices and the differences in energy between the His-containing and pure Ala helices, which we are calling the wire energy, WE.

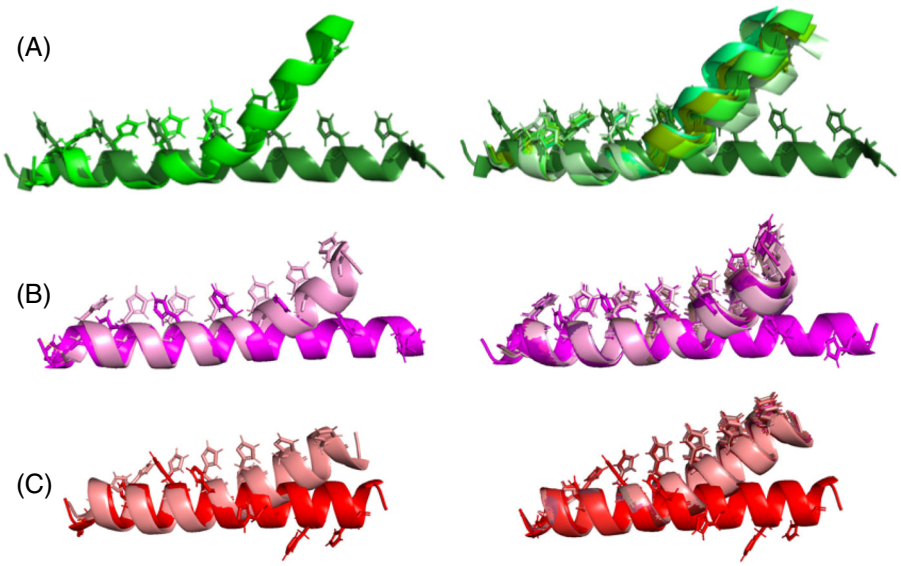

FIGURE 2 Representations of the seven-His initial (darkest shade on the bottom in each image) and fully optimized (lighter shades) structures for the 3_{10}-, α-, and π-helices (A, B, and C respectively). For the 3_{10}-helix residues 2–15 were used for alignment, and for the α-and π-helices residues 2–19 were used for alignment. Left: Fully optimized unprotonated structure. Right: Fully optimized unprotonated and all protonated (lighter shades) structures

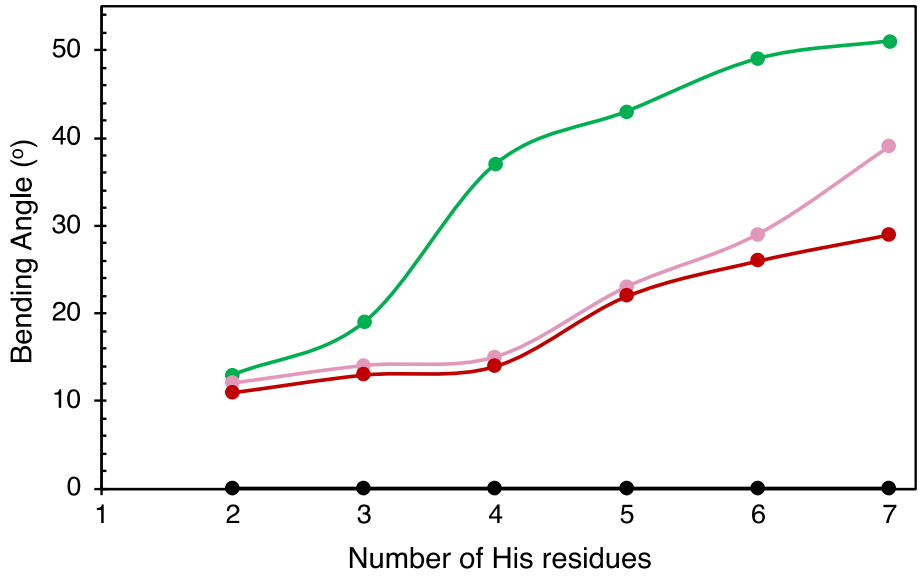

FIGURE 3 The bending angle of the initial helices (black) and optimized unprotonated 3_{10}- (green), α- (pink), and π-helices (red)

TABLE 2 Polymerization energies in kcal/mol for the unprotonated helices containing His, $\Delta E_{His,}$ and for pure poly-Ala helices, ΔE_{Ala}

Helix	Total number of residues	Number of His residues[a]	ΔE_{His} (kcal/mol)	ΔE_{Ala} (kcal/mol)	WE (kcal/mol)
3_{10}-	6	2	−3	−2	−1
	9	3	−14	−11	−3
	12	4	−24	−19	−5
	15	5	−36	−27	−9
	18	6	−44	−35	−9
	21	7	−54	−41	−13
α-	9	2	−5	8	−13
	13	3	−15	−1	−14
	17	4	−32	−11	−20
	21	5	−48	−22	−26
	25	6	−63	−34	−29
	29	7	−79	−48	−31
π-	11	2	7	9	−2
	16	3	−3	4	−7
	21	4	−13	−5	−8
	26	5	−26	−19	−7
	31	6	−38	−35	−3
	36	7	−51	−49	−2

Note: WE is the wire energy calculated as $\Delta E_{His} - \Delta E_{Ala}$.
[a]In the case of the pure Ala structures the His residues have been replaced with Ala residues to ensure the sequences have the same number of total residues.

In all cases, the stability increases almost linearly as the number of His residues increases. The negative values of ΔE_{HIS} indicate that all helices, except the π-helix with two His, are stable. In the case of ΔE_{Ala} all structures, except the α-helix with the equivalent of 2 His and the π-helix with the equivalent of 2 and 3 His, are stable. When helices with the same number of His residues are compared, the α-helices are the most stable, followed by the 3_{10}- and then the π-helices. This result agrees with our previous study of 21-residue helices [8].

When analyzing the WE, it is observed that WE <0 in all cases, which implies that the formation of the H-bond network (and thus the proton wire) stabilizes the helices. Specifically, the WEs for the α-helices are much larger than for the 3_{10}- and the π-helices—between 10 and

TABLE 3 Proton affinity (PA) and deprotonation energy (DE) when a proton was added to the N-terminus or extracted from the C-terminus, respectively

Helix	Total number of residues	Number of His	PA (kcal/mol)	DE (kcal/mol)
3_{10}-	6	2	265	18
	9	3	270	26
	12	4	272	29
	15	5	273	33
	18	6	273	38
	21	7	273	48
α-	9	2	260	24
	13	3	265	23
	17	4	264	27
	21	5	263	32
	25	6	262	39
	29	7	261	43
π-	11	2	260	15
	16	3	263	17
	21	4	261	22
	26	5	258	28
	31	6	257	33
	36	7	255	38

30 kcal/mol higher. Moreover, as the α- and 3_{10}- helices get longer, the WE increase, with larger increments observed for the longer α-helices. The WE in the π-helices are relatively small compared to those of 3_{10}- and α-helices.

Table 3 shows the proton affinity (PA) and desorption energy (DE) for all protonated helices considered. In all cases, the PA > 0, which implies that incorporating a proton into the helix is energetically favorable. The values range from 255 to 273 kcal/mol. This range is comparable to proton affinities observed experimentally for various peptides [28, 29].

The PA seems to be relatively size independent. In general, the 3_{10}- helices have about 10 kcal/mol higher PA than the α- and π-helices. Interestingly, the PA of the helices with one His are on the order of 260 kcal/mol in all cases. This is almost of the same magnitude as the PA of helices with multiple His residues, implying that additional His do not have a cooperative effect in stabilizing the proton that is being added. The fourth column of Table 3 shows the DE for each of the helices. As previously stated, this quantity tells us how much energy is needed to remove the proton after translocation through the wire. In general, DE values range from 15 to 48 kcal/mol, and in all cases, DEs increase as the number of His increase. No significant variation in DE was observed when comparing the various type of helices.

3.3 | PEC for proton translocation

Figure 4 shows the PEC for all the helices studied and Table 4 summarizes some of the important features of the PEC.

In all cases, no equilibrium structures were observed for the protonation of the first His (His_1). The first minimum was observed for protonation of the second His (His_2). The phenomenon occurs because the positively charged proton, when added to the first His, is repelled by the partial positive charge of the N-terminus. The separation between these two charges is between 6 and 9 Å (depending on the helix), hence a large coulombic repulsive force is generated. In addition, minima and transition states are localized for all systems, and in most cases, the energy decreases until the proton gets to the His_{N-1}, where *N* is the total number of His residues in the peptide.

From both Figure 4 and Table 4, it can be observed that the barriers (as determined from the time independent DFT calculations) are in the range of 1–5 kcal/mol and are independent of the size and nature of the helix. No pattern was observed for the energy barriers as the proton was translocated through a particular helix, for example, for the 3_{10} -helix with five His, the barriers are 3 kcal/mol, 1 kcal/mol, and 1 kcal/mol as the proton moves from His_2 to His_3 to His_4 to His_5, respectively. When Zero-point energy (ZPE) is considered, the vibrational energy in the ground state is ~2 kcal/mol for all cases. This indicates that the combination of zero-point vibrational energy and translational energy (RT@300 K = 0.6 kcal/mol) provides enough energy to surpass barriers that are less than 2.6 kcal/mol. Additionally, tunneling effects provide another mechanism to surpass the barrier. As previously stated, all transition states were characterized by calculating the imaginary frequency

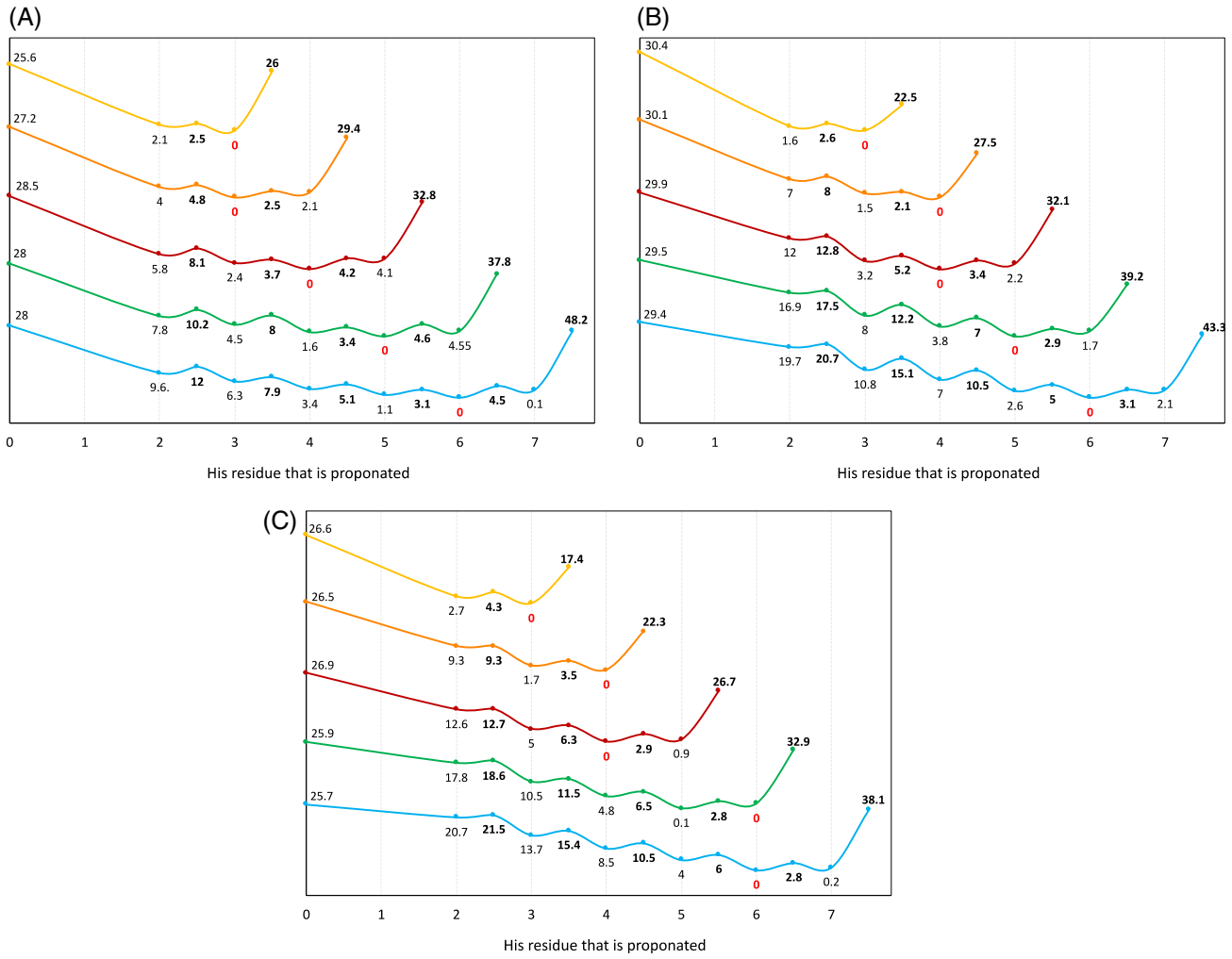

FIGURE 4 PEC for (A) 3_{10}-, (B) α-, and (C) π-helices. Energies are in kcal/mol and have been scaled to the lowest energy system on each helix.

($|v^{ts}|$) in the proton transport coordinate. It can be observed in the fifth column of Table 4 that there is a wide range in the values of $|v^{ts}|$, and no correlation between the size and/or type of helices is observed. The value of $|v^{ts}|$ provides a measurement of the probability for the proton to tunnel through a finite zero-point corrected barrier. As transition state frequencies increase, the probability of tunneling increases at a particular temperature and barrier [30]. Although no specific patterns are observed in $|v^{ts}|$, the longer helices seem to have a higher probability of tunneling, in particular at the end of the helices. No significant differences in $|v^{ts}|$ are observed between the different helices.

Finally, Table 4 shows the dipole moment (μ) for each of the systems studied. It is observed that as the helix gets longer, μ increases—with higher μ for the π-, followed by the α- and then the 3_{10}- helices. Interestingly, the main component of the dipole moment lies in the x-axis, which is the axis where the dipole moment points from the N-terminus to the C-terminus (along which the helical axis is aligned). It is this component of the dipole moment that controls the potential unidirectional translocation of the proton. Interestingly, no correlation is observed between μ or μ_x of the helices and the size of the barriers or the proton affinities. As μ increases, however, the deprotonation energy increases. Therefore, increasing μ does not change the PEC or the affinity of the helix for the proton, but it increases the amount of energy necessary to remove the proton from the helix. Because of the low energy barriers observed in the proton translocation and the high deprotonation energies, it is reasonable to conclude that the efficiency of the wires is deprotonation controlled.

In order to characterize the dynamics of proton translocation and be certain that the proton transfer is indeed fast (as suggested by the low energy barriers) and unidirectional (as suggested by the macroscopic dipole moment in the x-direction), AIMD simulations were performed at $T = 300$ K (to account for temperature effects) for the α-helix with four and seven His residues. We have chosen the α-helix for this study because of the high stability and large proton affinity obtained and because it has been shown that these peptides are relatively simple and inexpensive to synthesize experimentally [31]. The initial configuration used was the equilibrium structure obtained for this helix protonated in His_2. Throughout the simulation, the secondary structure of the helix is conserved.

TABLE 4 Range of energy barriers (EB), the magnitude of the imaginary frequency of the transition state ($|\nu^{ts}|$), dipole moments (μ), and μ_x component of the dipole moment along the x-axis for the 3_{10}- α-, and π-helices when protonation occurs on the second His

Helix	Total number of residues	Number of His	Range of EB (kcal/mol)	$\lvert\nu^{ts}\rvert$ (cm^{-1})	μ (Debye)	μ_x (Debye)
3_{10}-	6	2			19	15
	9	3	1	817	39	35
	12	4	1–3	533–781	52	50
	15	5	1–4	222–862	68	66
	18	6	1–5	267–916	82	81
	21	7	1–3	297–940	96	95
α-	9	2			31	26
	13	3	1	839	46	44
	17	4	1	718–900	68	66
	21	5	1–3	591–928	87	86
	25	6	1–4	458–924	109	108
	29	7	1–4	747–983	126	124
π-	11	2			30	27
	16	3	2	706	57	55
	21	4	1–2	235–928	82	82
	26	5	1–3	462–998	109	107
	31	6	1–3	323–998	135	135
	36	7	1–3	429–1007	162	162

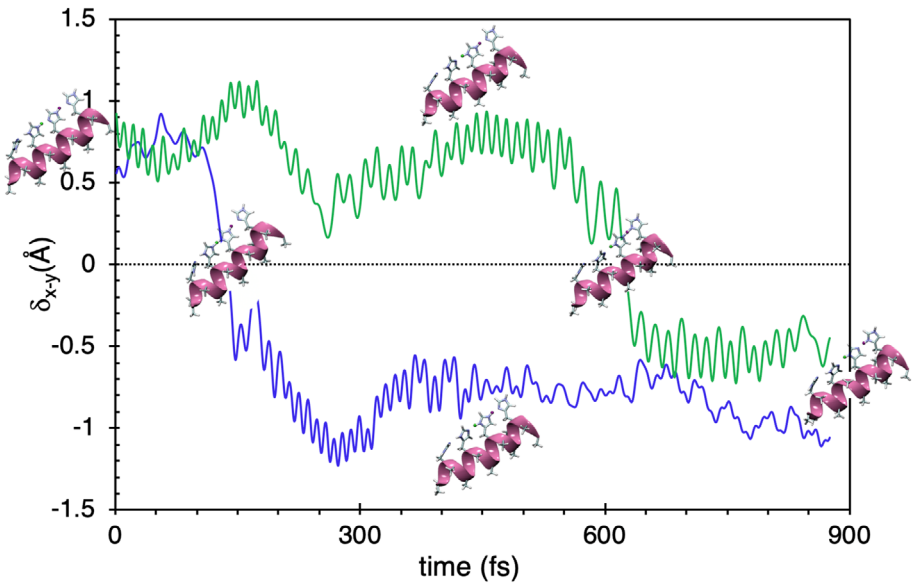

FIGURE 5 Variation in two sharing proton coordinates as a function of time for the α-helix containing four His residues. The green curve corresponds to δ_{2-3} and the green curve corresponds to δ_{3-4}.

Figure 5 shows the variation in two sharing proton coordinates, defined as δ_{x-y} (where x and y refer to adjacent HIS residues, Figure S3) as a function of time for the α-helix with four His. The green and blue curves refer to δ_{2-3} and δ_{3-4}, respectively. Table 5 shows the time that is required for the proton to pass through each transition state. From Figure 5, at t < 130 fs, δ_{2-3} and δ_{3-4} > 0, implying that the initial protonated equilibrium structure is preserved. At t ~ 137 fs, $\delta_{2-3} = 0$, implying that the proton reached the transition state between His_2 and His_3, and at t ~ 180 fs, δ_{2-3} < 0 the proton is transferred to His_3. The proton now located in His_3 reaches the transition state between His_3 and His_4 at t ~ 625 fs and is transferred quickly to His_4, that is, at t ~ 640 fs. No re-crossing dynamics of the transition states are observed.

TABLE 5 Time in femtoseconds (t_{x-y}) for proton the excess proton to pass the transition state between x and y for the α-helixes containing 4 and 7 His residues

System	t_{2-3}	t_{3-4}	t_{4-5}	t_{5-6}	t_{6-7}
4-His	137	625			
7-His	157	577	659	740	Not observed

Note: This time is determined when $\delta_{x-y} < 0$ for the first time.

TABLE 6 Energy barriers (kcal/mol) for the forward and backward proton transfer in the α-helices containing 4 and 7 His residues

	Barrier (kcal/mol)									
	Forward direction					Backward direction				
System	$H_{2\to3}$	$H_{3\to4}$	$H_{4\to5}$	$H_{5\to6}$	$H_{6\to7}$	$H_{7\to6}$	$H_{6\to5}$	$H_{5\to4}$	$H_{4\to3}$	$H_{3\to2}$
4-His	1	1	-	-	-	-	-	-	2	7
7-His	1	4	4	2	3	1	5	8	8	10

From Table 5, it can also be seen that the translocation of the proton in the seven His helix is very similar to the previously discussed dynamics in the four His helix. Namely, the proton is transferred in the direction of the helical axis in the fs timescale. Translocation from His_2 to His_3 is approximately the same as in the four His helix, and translocation from His_4 to His_5 is faster in the seven His helix than in the four His helix (48 fs faster). The remaining transitions all occur within 1021 fs. Similar to the four His helix, no re-crossing dynamics of the transition states are observed, suggesting that the directionality of the proton transfer is guided by the macroscopic dipole moment of the helix. These results confirm that the proton translocation is both fast and potentially unidirectional (in the direction of the dipole moment), as predicted from the constructed PEC for the proton translocation. Our dynamical results suggest that proton transport might occur in a unidirectional fashion, but this is not proved.

Table 6 shows the proton transport barriers in the forward and backward directions for the α-helices containing 4- and 7-His residues. It can be seen that in general for these systems the forward barriers are lower than the backward barriers suggesting that the backward proton transfer is less favorable (in accordance with the non-observation of re-crossing dynamics above). For the7-His system however, the barrier for the $H_{7\to6}$ is smaller than the barrier for the $H_{6\to7,}$ suggesting that the proton can go back to the 6th residue, but is unlikely to move beyond that. This explains why the t_{6-7} is not observed above.

It should be noted however, that while the size of the backward barriers suggests that the backward proton transport is less likely, it does not prove that this process is kinetically unfavorable. Moreover, the non-observation of re-crossing dynamics in the AIMD simulations (which support this idea) might in fact be due to the short simulation times. To unequivocally demonstrate that the proton transport is unidirectional would require the use of a kinetic model and the quantification of proton transport steps in opposite directions. As an example, kinetic Monte Carlo models have been designed to describe proton translocation in quasi-one-dimensional systems [32, 33]. At present, we are designing such a model using the structural and energy barriers obtained in this study.

4 | CONCLUSION

In this study, we have computationally constructed and optimized and then obtained detailed structural and energetic information for His-containing 3_{10}-, α-, and π-helices of varying lengths. Despite distortions in the backbone, all three types of helical conformations conserve their respective secondary structure and are energetically stable, with the α- being more stable than the 3_{10}- and the π. In all three cases, increasing the length of the helices results in an increase the stability, potentially due to the increased macroscopic dipole moment. In addition, the alignment of the His residues (due to the bending) results in the formation of a H-bond network (or proton wire) that stabilizes the systems, irrespective of secondary structure or length. Notably, the 3_{10}-helix shows the largest bending angle, potentially making it the least appropriate for further investigation.

No significant changes are observed in the structure of the helices upon protonation, and protonated helices have PAs between 260 and 273 kcal/mol (which is independent of size) and DEs of 15–49 kcal/mol. Interestingly, the DEs increase with the length of the helices, with the α- helix showing the smallest range. These values can be compared with Auerbach's work on imidazoles, where the PAs are in the range of 160–230 kcal/mol and the DE's are on the order of 25 kcal/mol [6]. The higher PA and lower DE of our systems imply that these non-aqueous His-containing peptides form efficient proton wires. As the proton is translocated through the wire the energy of the systems decreases until the

second to last His residue (from N-terminus to C-terminus) is protonated. Translocation barriers between 1 and 4 kcal/mol are obtained, as compared to barriers of 2.5 kcal/mol obtained by Auerbach, again implying that these systems are comparable in terms of proton transfer.

In all cases, correction for zero-point energy decreases the barriers by ~2 kcal/mol, indicating that the combination of zero-point vibrational energy and translational energy (RT@300 K = 0.6 kcal/mol) provides enough energy to surpass barriers that are less than 2.6 kcal/mol. The magnitude of $|v^{ts}|$, in the transition state suggests that tunneling effects might be important in proton translocation, in particular at the end of the helices. AIMD results suggest that a proton could be shuttled unidirectional through two His residues in ~1 ps. In general, these systems exhibit high proton affinities, low energy barriers, and high deprotonation energies, suggesting that the deprotonation is the rate-limiting step in the efficiency of the wires.

This work shows that the longer the peptide (21–36 residues), the faster the potentially unidirectional proton transfer, suggesting that longer H-bonded networks within a dipole-containing material will produce highly efficient proton transfer. These peptides then can be combined with other nanomaterials that contain channels within which proton transfer has been shown to occur upon the application of an external current (with comparable barriers), to create a composite material that can facilitate proton transfer without the need for the external driving force. Specifically, the diameter of these channels is on the order of 8 Å and the peptides studied here have a diameter of 6–8 Å.

AUTHOR CONTRIBUTIONS

Jiang Bian: Data curation; formal analysis; investigation; visualization; writing – original draft; writing – review and editing. **Anthony Cruz:** Conceptualization; formal analysis; investigation; methodology; software; visualization. **Gabriel López-Morales:** Investigation; methodology; software. **Anton Kyrylenko:** Data curation; investigation; validation. **Donna McGregor:** Data curation; formal analysis; investigation; supervision; writing – original draft; writing – review and editing. **Gustavo E. López:** Conceptualization; data curation; formal analysis; funding acquisition; investigation; methodology; project administration; resources; software; supervision; validation; visualization; writing – original draft; writing – review and editing.

ACKNOWLEDGMENT

NSF CREST Center for Interface Design and Engineered Assembly of Low Dimensional Materials (IDEALS) grant number HRD–1547830. NIH/SCORE under award number 1SC3GM139673.

DATA AVAILABILITY STATEMENT

The data that supports the findings of this study are available within the article and its Supporting Information.

ORCID

Gustavo E. López https://orcid.org/0000-0003-1660-547X

REFERENCES

[1] L. G. Lage, P. G. Delgado, Y. Kawano, *J. Therm. Anal. Calorim.* **2004**, *75*, 521.
[2] T. Stahl, D. Mattern, H. Brunn, *Environ. Sci. Eur.* **2011**, *23*, 38.
[3] C. J. T. de Grotthuss, *Ann. Chim.* **1806**, *58*, 54.
[4] J. F. Nagle, H. J. Morowitz, *Proc. Natl Acad. Sci. USA* **1978**, *75*(1), 298.
[5] N. Agmon, *Chem. Phys. Lett.* **1995**, *244*, 456.
[6] U. Viswanathan, D. Basak, D. Venkataraman, J. T. Fermann, S. M. Auerbach, *J. Phys. Chem. A* **2011**, *115*, 5423.
[7] J. Li, Z. Wu, H. Li, H. Liang, S. Li, *New J. Chem.* **2018**, *42*(3), 1604.
[8] U. Sen, S. Unugurcelik, A. Ata, A. Bozkurt, *Int. J. Hydrogen Energy* **2008**, *33*(11), 2808.
[9] X. Li, H. Zhang, H. Yu, J. Xia, Y. Zhu, H. Wu, J. Hou, J. Lu, R. Ou, C. D. Easton, C. Selomulya, M. R. Hill, L. Jiang, H. Wang, *Adv. Mater.* **2020**, *32*(24), 2001777.
[10] G. E. López, I. Colón-Díaz, A. Cruz, S. Ghosh, S. B. Nicholls, U. Viswanathan, J. A. Hardy, S. M. Auerbach, *J. Phys. Chem. A* **2012**, *116*, 1283.
[11] Z. Long, A. O. Atsango, J. A. Napoli, T. E. Markland, M. E. Tuckerman, *J. Phys. Chem. Lett.* **2020**, *11*(15), 6156.
[12] D. Marx, *ChemPhysChem* **2006**, *7*(9), 1848.
[13] Dassault Systèmes BIOVIA, *Discovery Studio Modeling Environment*, *Release 2017*, Dassault Systèmes, San Diego, CA **2016**.
[14] M. J. Frisch, G. W. Trucks, H. B. Schlegel, G. E. Scuseria, M. A. Robb, G. Cheeseman Scalmani, V. Barone, G. A. Peterrson, H. Nakatsuji, X. Li, M. Caricato, A. Marenich, J. Bloino, B. G. Janesko, R. Gomperts, B. Mennucci, H. P. Hratchian, J. V. Ortiz, A. F. Izmaylov, J. L. Sonnenberg, D. Williams-Young, F. Ding, F. Lipparini, F. Egidi, J. Goings, B. Peng, A. Petrone, T. Henderson, D. Ranasinghe, V. G. Zakrzewski, J. Gao, N. Rega, G. Zheng, W. Liang, M. Hada, M. Ehara, K. Toyota, R. Fukuda, J. Hasegawa, M. Ishida, T. Nakajima, Y. Honda, O. Kitao, T. Nakai, T. Vreven, K. Throssell, J. A. Montgomery Jr., J. E. Peralta, F. Ogliaro, M. Bearpark, J. J. Heyd, E. Brothers, K. N. Kudin, V. N. Staroverov, T. Keith, R. Kobayashi, J. Normand, K. Raghavarachi, A. Rendell, J. C. Burant, S. S. Iyengar, J. Tomasi, M. Cossi, J. M. Millam, M. Klene, C. Adamo, R. Cammi, J. W. Ochterski, R. L. Martin, K. Morokuma, O. Farkas, J. B. Foresman, D. J. Fox, *Gaussian 09*, Gaussian Inc., Wallingford, CT **2016**.
[15] M. Mezei, M. Filizola, *J. Comput.-Aided Mol. Des.* **2006**, *20*, 97.
[16] M. Mezei, *J. Comput. Chem.* **2010**, *31*, 2658.
[17] W.L. DeLano, The PyMOL molecular graphics system 2002. http://www.pymol.org

[18] C. Peng, P. Y. Ayala, H. B. Schlegel, M. J. Frisch, *J. Comput. Chem.* **1996**, *17*(1), 49.
[19] K. Tao, J. O. Donnell, H. Yuan, U. Haq Ehtsham, S. Guerin, L. J. W. Shimon, B. Xue, C. Silien, Y. Cao, D. Thompson, R. Yang, S. A. M. Tofail, E. Gazit, *Energy Environ. Sci.* **2020**, *13*(1), 96.
[20] P. Losch, H. R. Joshi, O. Vozniuk, A. Grünert, C. Ochoa-Hernández, H. Jabraoui, M. Badawi, W. Schmidt, *J. Am. Chem. Soc.* **2018**, *140*(50), 17790.
[21] F. L. Brancia, M. Stener, A. Magistrato, *J. Am. Soc. Mass Spectrom.* **2009**, *20*(7), 1327.
[22] H.-J. Leem, I. Dorbandt, J. Rojas-Chapana, S. Fiechter, H. Tributsch, *J. Phys. Chem. C* **2008**, *112*(7), 2756.
[23] P. E. Blöchl, *Phys. Rev. B* **1994**, *50*(24), 17953.
[24] G. Kresse, J. Furthmüller, *Phys. Rev. B* **1996**, *54*(16), 11169.
[25] J. P. Perdew, M. Ernzerhof, K. Burke, *J. Chem. Phys.* **1996**, *105*(22), 9982.
[26] S. Grimme, J. Antony, S. Ehrlich, H. Krieg, *J. Chem. Phys.* **2010**, *132*(15), 154104.
[27] S. Aravinda, N. Shamala, I. L. Karle, P. Balaram, *Biopolymers* **2012**, *98*(1), 76.
[28] Z. Wu, C. Fenselau, *J. Am. Soc. Mass Spectrom.* **1992**, *3*(8), 863.
[29] L. Sterner, V. Johnston, R. Nicol, P. Ridge, *J. Am. Soc. Mass Spectrom.* **1999**, *10*, 483.
[30] J. Fermann, S. Auerbach, *J. Chem. Phys.* **2000**, *112*, 6787.
[31] Z. Song, H. Fu, J. Wang, J. Hui, T. Xue, L. A. Pacheco, H. Yan, R. Baumgartner, Z. Wang, Y. Xia, X. Wang, L. Yin, C. Chen, J. Rodríguez-López, A. L. Ferguson, Y. Lin, J. Cheng, *Proc. Natl. Acad. Sci. USA* **2019**, *116*(22), 10658.
[32] G. Kabbe, C. Wehmeyer, D. Sebastiani, *J. Chem. Theory Comput.* **2014**, *10*(10), 4221.
[33] T. Masłowski, A. Drzewiński, J. Ulner, J. Wojtkiewicz, M. Zdanowska-Frączek, K. Nordlund, A. Kuronen, *Phys. Rev. E* **2014**, *90*(1), 012135.

SUPPORTING INFORMATION

Additional supporting information can be found online in the Supporting Information section at the end of this article.

How to cite this article: J. Bian, A. Cruz, G. López-Morales, A. Kyrylenko, D. McGregor, G. E. López, *Int. J. Quantum Chem.* **2022**, *122*(19), e26964. https://doi.org/10.1002/qua.26964